Chemical Science

ROYAL SOCIETY OF CHEMISTRY

EDGE ARTICLE

View Article Online
View Journal | View Issue

Cite this: *Chem. Sci.*, 2023, **14**, 937

All publication charges for this article have been paid for by the Royal Society of Chemistry

A theoretical framework for the design of molecular crystal engines†

Cameron J. Cook,[a] Wangxiang Li,[a] Brandon F. Lui,[a] Thomas J. Gately,[a] Rabih O. Al-Kaysi,[b] Leonard J. Mueller,[a] Christopher J. Bardeen[a] and Gregory J. O. Beran *[a]

Received 6th October 2022
Accepted 19th December 2022

DOI: 10.1039/d2sc05549j

rsc.li/chemical-science

Photomechanical molecular crystals have garnered attention for their ability to transform light into mechanical work, but difficulties in characterizing the structural changes and mechanical responses experimentally have hindered the development of practical organic crystal engines. This study proposes a new computational framework for predicting the solid-state crystal-to-crystal photochemical transformations entirely from first principles, and it establishes a photomechanical engine cycle that quantifies the anisotropic mechanical performance resulting from the transformation. The approach relies on crystal structure prediction, solid-state topochemical principles, and high-quality electronic structure methods. After validating the framework on the well-studied [4 + 4] cycloadditions in 9-methyl anthracene and 9-*tert*-butyl anthracene ester, the experimentally-unknown solid-state transformation of 9-carboxylic acid anthracene is predicted for the first time. The results illustrate how the mechanical work is done by relaxation of the crystal lattice to accommodate the photoproduct, rather than by the photochemistry itself. The large $\sim 10^7$ J m^{-3} work densities computed for all three systems highlight the promise of photomechanical crystal engines. This study demonstrates the importance of crystal packing in determining molecular crystal engine performance and provides tools and insights to design improved materials *in silico*.

1 Introduction

Organic photomechanical crystals transform light into mechanical work *via* the changes in solid-state structure that result from a photochemical reaction.[1] These structural changes can induce elongation, bending, twisting, photosalience, and other behaviors.[2–5] While numerous examples of photomechanical behaviors can be found in the literature,[6–14] a predictive understanding of the relationships between molecular structure, crystal packing, photochemical transformation, and the mechanical work output remains elusive. Such understanding is vital for the rational design of photomechanical engines based on molecular crystals.[15]

In principle, determining the work output of a light-induced crystal-to-crystal transformation should be straightforward. In practice, photomechanical crystals present specific challenges that have so far prevented the development of a comprehensive theoretical framework. First, it is often difficult to determine the structure of the product crystal after photoreaction. Performing solid-state photochemical reactions in bulk crystals often causes them to shatter, complicating diffraction experiments.[6,16,17] If the photoproduct absorbs strongly at the excitation wavelength (positive photochromism), then a photostationary state is reached and complete conversion is impossible. To circumvent this problem, one might isolate the photoproduct in solution and recrystallize it. Unfortunately, the product crystal grown in this manner may have a different crystal packing from that formed by direct photoconversion in the solid-state.[18] Finally, if the reaction is thermally reversible (T-type), the photoproduct may be too short-lived for practical structure determination. Progress in measuring experimental work outputs directly has been made recently,[13] though such techniques are not yet widespread.

Even if the photoproduct crystal structure can be determined experimentally, this leads to a second, more fundamental challenge: how does the transformation from the reactant to the product crystal actually occur? As with gas expansion cycles in thermodynamics, this process should consist of a series of well-defined steps, each of which can be associated with an energy change. To simplify the problem, we will concentrate on

[a]*Department of Chemistry, University of California Riverside, Riverside CA 92521, USA. E-mail: gregory.beran@ucr.edu*

[b]*College of Science and Health Professions-3124, King Saud Bin Abdulaziz University for Health Sciences, and King Abdullah International Medical Research Center, Ministry of National Guard Health Affairs, Riyadh 11426, Kingdom of Saudi Arabia*

† Electronic supplementary information (ESI) available: Additional computational details, experimental methods and data, crystal structure prediction results, comparisons of predicted and experimental crystal structures, and tabulation of the unit transformations and maximum computed work densities. See DOI: **https://doi.org/10.1039/d2sc05549j**

complete conversion of the reactant to product that gives rise to crystal expansion and contraction. It should be noted that the most commonly reported mode of photomechanical crystal actuation involves bending due to partial conversion that yields a reactant–product bimorph structure.[19–21] In principle, a bending crystal can be divided into subdomains that undergo expansion/contraction after complete conversion, so this approach should be general and adaptable to bending as well.

The significant experimental and conceptual challenges in this field motivated us to turn to computational chemistry to predict the structures, transformations, and properties of photomechanical crystals entirely from first-principles. Organic molecular crystal structure prediction has advanced considerably in recent years, thanks in large part to the development of accurate and computationally efficient electronic structure models for the solid state,[22–25] which have considerably enhanced researchers' abilities to predict the thermodynamically most stable polymorphs.[26–44] As a result, successful examples of crystal structure predictions in the Blind Tests,[45–47] pharmaceuticals,[48–52] and organic materials[53–60] are accumulating rapidly.

Successful application of crystal structure prediction to photomechanical crystals would enable first-principles design and optimization of this promising class of materials. Unfortunately, this effort faces two major challenges. First, instead of generating the landscape of candidate structures for a single species, as in traditional crystal structure prediction, predicting a solid-state photomechanical response requires understanding the structures and transformations between two distinct crystal energy landscapes (reactant and product). Second, energetic stability cannot be the primary criterion for identifying the photochemical polymorph produced by the solid-state reaction. High photon energy and the steric constraints created by the solid-state reaction environment can drive the reaction toward a high-energy, thermodynamically metastable product.[61] In other words, the conventional crystal structure prediction goal generating a modest number of low-energy polymorphs is replaced by the challenge of identifying the relevant structure(s) from a much larger pool of higher-energy candidate structures.

Here, we develop a new, first-principles methodology for predicting solid-state molecular crystal photomechanical transformations that overcomes these difficulties. It generates structures using crystal structure prediction, employs a crystalline topochemical hypothesis to predict the solid-state photochemical transformations, and establishes a photomechanical engine cycle that characterizes the anisotropic work produced by the structural changes. This theoretical approach is validated on two well-characterized [4 + 4] anthracene derivative photodimerization systems (**9MA** and **9TBAE**, Fig. 1). This negative photochromic reaction permits complete conversion of the crystals to a stable photodimer form, avoiding mixtures and facilitating comparison to theory. We also use the theory to predict the photodimer crystal structure of a T-type reversible crystal (**9AC**) that has not yet been measured experimentally but may be more practical for actuator applications. The large $\sim 10^7$ J m^{-3} work densities computed for all three systems demonstrate the exceptional promise of organic molecular crystal engines. Moreover, our findings demonstrate how molecular crystal packing plays a key role in determining the anisotropic work generated, emphasizing the value of theoretical tools capable of characterizing the stress and strain generated in these transformations.

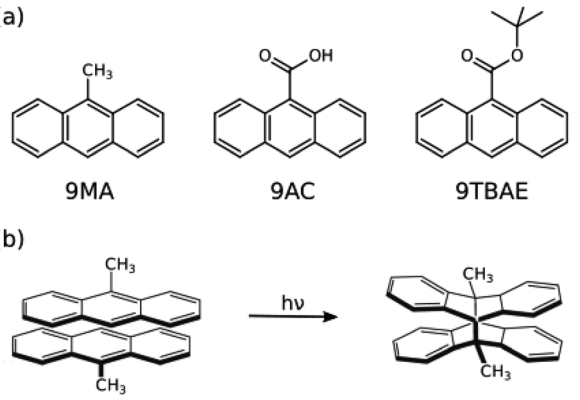

Fig. 1 (a) The structures of 9-methyl anthracene (**9MA**), 9-anthracene carboxylic acid (**9AC**), and 9-*tert*-butyl anthracene ester (**9TBAE**). (b) The [4 + 4] photodimerization reaction of **9MA**. The solid-state photochemical transformations have been established experimentally for **9MA** and **9TBAE**, but not for **9AC**.

2 Methods

2.1 Crystal structure prediction for 9MA

After optimizing the gas-phase monomer and photodimer structures using B3LYP/6-311+G(d)[62] in Gaussian09,[63] candidate crystal structures for the monomer and photodimer were generated from first-principles *via* a hierarchical crystal structure prediction protocol. For each species, 55 000 crystal structures from 11 common space groups were randomly generated using PyXtal,[64] assuming a single molecule in the asymmetric unit ($Z' = 1$). These crystal structures were relaxed using the Generalized Amber Force Field (GAFF)[65] in CHARMM 45b2[66] and clustered to eliminate duplicates.

Next, all 281 monomer crystal structures lying within 10 kJ mol^{-1} of the lowest-energy structure, and all 255 photodimer crystal structures within 25 kJ mol^{-1} were further relaxed with the semi-empirical HF-3c method[67] as implemented in CRYSTAL17.[68] The higher energy cutoff for the photodimer landscape was chosen due to the relative sparsity of structures compared to the monomer landscape and the expectation that the SSRD could lie relatively high in energy. HF-3c refinement and another round of structure clustering reduced the landscape to 63 monomer structures within 10 kJ mol^{-1} and 42 photodimer structures within a 15 kJ mol^{-1} energy window. Final refinement of those crystal structures was performed using planewave density functional theory (DFT), using the van der Waals-corrected B86bPBE-XDM functional[69–71] in QuantumEspresso.[72]

Energy relationships between the monomer and photodimer landscapes were computed according to,

$$2\ \mathbf{9MA} \rightarrow (\mathbf{9MA})_2 \quad (1)$$

However, conventional density functionals used in solid-state calculations describe the anthracene photodimerization poorly.[61,73–75] The issue stems from delocalization error in the approximate density functionals,[76] which artificially stabilizes extended π delocalization found in the anthracene monomer by dozens of kJ mol^{-1} relative to the photodimer with sp^3-hybridized carbon centers and more localized electron density (Fig. 1).[61,74,75] Issues arising from DFT delocalization error have been identified in a number of other organic crystals as well.[28,42–44,77–80]

To address the delocalization error issues inherent in B86bPBE-XDM (and other density functionals) for these systems, an intramolecular correction is applied to all periodic DFT lattice energies. This single-point energy correction replaces the intramolecular energies of the monomer or photodimer with more accurate ones computed at the spin-component-scaled dispersion-corrected second-order Møller–Plesset perturbation theory (SCS-MP2D)[75] level,

$$E_{\text{crystal}} = E^{\text{DFT}}_{\text{crystal}} + \sum_{i=1}^{Z}\left(E^{\text{SCS-MP2D}}_{\text{molec},i} - E^{\text{DFT}}_{\text{molec},i}\right) \quad (2)$$

The molecular energies on the right-hand side are computed in the gas-phase using geometries extracted directly from the DFT-optimized crystal. The sum runs over all Z molecules in the unit cell, though space group symmetry can be exploited to compute the gas-phase molecular energies only for the molecules in the asymmetric unit. This correction has been employed successfully in several other systems.[43,44,61,79] SCS-MP2D reproduces the benchmark coupled cluster single, doubles, and perturbative triples (CCSD(T)) anthracene photodimerization reaction energy to within 1.2 kJ mol^{-1}.[75] Further computational details of the crystal structure prediction can be found in ESI Section S1.†

2.2 Topochemical identification of the solid-state reacted structures

Characterizing the photomechanical transformation and the associated work performed requires identifying the solid-state reacted dimer (SSRD) crystal structure which results from the solid-state reaction. This is done topochemically, replacing the reacting monomer pairs in the monomer crystal structure with photodimers placed at the same center of mass positions and oriented to maximize overlap with the original monomer pair. Constrained DFT geometry optimization of the replaced molecules within the fixed monomer lattice parameters produces the "proto-SSRD," while subsequent variable-cell relaxation produces the equilibrium SSRD structure. Similarly, one can construct the "proto-monomer" for the reverse dissociation reaction by substituting monomers into the photodimer unit cell. See the Results section and ESI Section S1.2† for more details.

2.3 Work density calculations

The elastic work density is evaluated from the DFT-computed Cartesian stress (σ) and strain (ε) tensors for the proto-SSRD/proto-monomer relative to their fully-relaxed equilibrium structures. Tight DFT geometry-optimization criteria were employed to improve convergence of the stress and strain tensors. The orientational dependence of the work density, including both normal and shear contributions, was computed by projecting it onto different crystallographic directions defined by the unit vector n̂.

$$W(\hat{n}) = \frac{1}{2}\hat{n}^{\mathrm{T}}\sigma\varepsilon\hat{n} \quad (3)$$

After scanning over all directions n̂, the absolute value of the work densities (in MJ m^{-3}) are plotted as a heat map on the surface of a sphere. Examination of the **9MA** proto-SSRD relaxation finds the stress to vary nearly linearly with strain, supporting the assumption of elastic work. See ESI Section S1.3† for further details on the work calculations.

Ref. 13 and 81 present several performance metrics that can be used to assess an actuator, including the work output (maximum force times the displacement), work capacity ($W_{\text{capacity}} = \sigma_{\max}\varepsilon_{\max}$), and the power output (work output per unit of time). The work densities computed in eqn (3) are very similar to their work capacity, though the work densities here examine the anisotropic work in various possible directions, rather than focusing on a specific actuator geometry. Consideration of process timescales and power are beyond the scope of this study.

Experimental methods are described in ESI Section S2.†

3 Results and discussion

3.1 Crystal structure prediction of key intermediates for the photomechanical cycle

The crystal energy landscape for photomechanical materials based on the anthracene [4 + 4] photodimerization will typically contain at least three notable structures: the reactant crystal, a polymorph of the photochemical product crystallized from solution (referred to as the solution-grown dimer, or SGD), and the SSRD polymorph generated through the solid-state crystal-to-crystal photochemical reaction. The SSRD is central to the photomechanical process, and we hypothesize that the SGD and SSRD crystal structures will match only in rare cases. Our first task is to identify and characterize these structures. The monomer reactant and SGD product will frequently be the thermodynamically most stable polymorphs on their respective landscapes, while the SSRD lies quite a bit higher in energy.

3.1.1 9MA. For **9MA**, the initial force-field-level crystal structure prediction landscapes contain the experimental monomer and SGD structures, though the monomer lies ∼6 kJ mol^{-1} higher than the most stable predicted monomer crystal, while the SGD is the second-most stable form on its landscape at +0.1 kJ mol^{-1}. However, further refinement of the landscapes with increasingly accurate levels of theory shifts the **9MA** monomer and SGD to become the global minimum energy structures on their respective crystal structure landscapes (ESI Fig. S5 and S6†). After correcting for the ∼60 kJ mol^{-1} intramolecular DFT delocalization error with SCS-MP2D according to eqn (2), the monomer and SGD crystals become nearly isoenergetic (Fig. 2).

The predicted monomer and SGD structures match the experimentally reported crystal structures[82] with excellent overlaps of 0.20–0.23 Å using the 15-molecule cluster root-mean-square deviation (rmsd15) metric (Fig. 2).[83] The DFT unit cell parameters for the **9MA** monomer and SGD are only 1.2% smaller than the experimental ones on average (ESI Table S3†), which is consistent with the underestimation of unit cell volumes expected for comparing 0 K DFT calculations to room-temperature experimental structures.[84]

While the ability to predict the thermodynamically most stable polymorphs of **9MA** and its photodimer correctly is important, understanding the crystal-to-crystal transformation associated with the photomechanical response also requires identifying the SSRD polymorph on the photodimer crystal energy landscape. Energetic stability alone cannot be used as a criterion for the SSRD, since the constraints of the solid-state reaction environment can produce an SSRD that is highly metastable.[61] A similar focus on high-energy structures occurs when predicting structures of porous organic materials,[56,57,60] though there it stems from the models' omission of guest/solvent molecules which stabilize the pores experimentally.

A key conceptual advance in this paper lies in extending the topochemical principle to the problem of predicting the photoproduct crystal structure, rather than just the photoproduct molecule by itself. Solid-state anthracene [4 + 4] photodimerization reactions only occur when the reactive carbon atoms lie within 4.2 Å and satisfy various orientational constraints.[85–87] Moreover, the steric constraints imposed by the crystalline lattice limit molecular reorganization after the photochemical transformation, thereby constraining the photoproduct crystal structure and inhibiting its relaxation to the lowest-energy SGD packing. Therefore, instead of relying on an energetic stability criterion, we identify the SSRD based on the crystal packing relationships that connect structures between the monomer and photodimer crystal energy landscapes.

Specifically, we predict the product of the crystal-to-crystal transformation with no experimental information by generating an initial topochemical SSRD crystal in which the reacting monomer pairs in the predicted monomer crystal are replaced by photodimer molecules having the same positions and orientations, as described in ESI Section S1.2.† Constrained DFT relaxation of this crystal structure with the lattice vectors held fixed at their monomer crystal values produces the proto-SSRD. Subsequent unconstrained relaxation of the proto-SSRD atoms and lattice vectors produces the final equilibrium SSRD structure. Applying this procedure to **9MA** (Fig. 3a), we find that the SSRD retains the same $P2_1/c$ space group as the reactant monomer crystal, and it matches the rank #27 structure on the DFT photodimer crystal structure prediction landscape (Fig. 2) with an excellent rmsd15 overlap of 0.14 Å.

Determining the **9MA** SSRD crystal structure experimentally is difficult, since bulk crystals fracture after about ~30% photodimerization under ambient conditions.[88] Turowska-Tyrk and coworkers recently showed that photodimerization of single **9MA** crystal can be carried to completion without fracture at elevated pressures in a diamond anvil cell.[85] The SSRD structure predicted here (at 0 GPa) is an outstanding match for the experimental X-ray crystal structures reported at 0.1 and 0.4 GPa, with rmsd15 values of only 0.12 Å (Fig. 2).

Morimoto *et al.* observed that single microcrystal plates could expand by a factor of 1.07 along their *c*-axis while remaining intact.[89] Presumably, these crystals also adopt the SSRD structure after conversion. To confirm this, we performed powder X-ray diffraction (PXRD) experiments on **9MA** microplates after photodimerization. Fig. 4 compares the experimental PXRD pattern with a simulated one for the predicted SSRD structure. The microplates were not powdered, so their

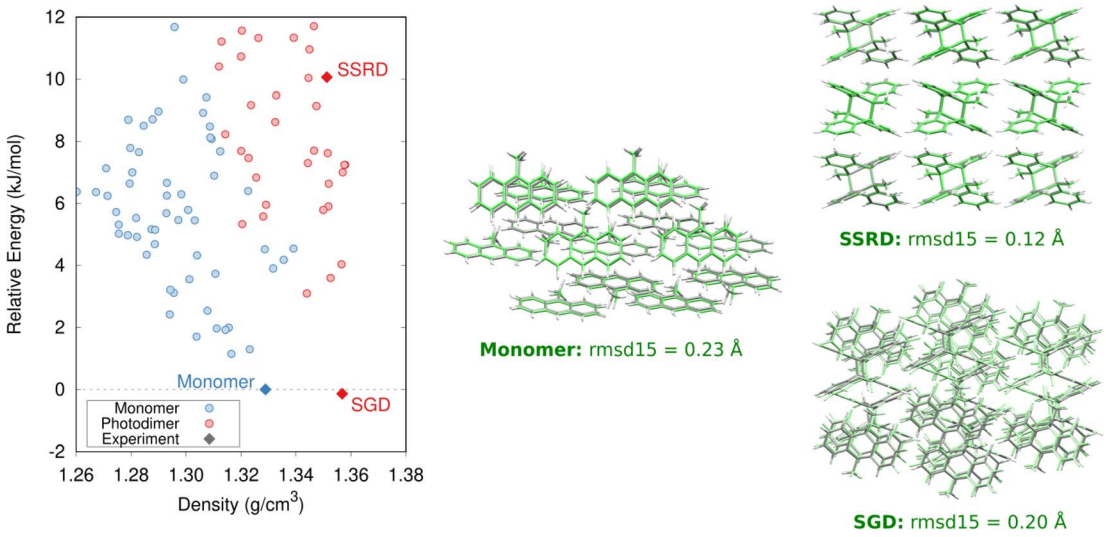

Fig. 2 Predicted crystal energy landscape for the 9MA monomers and photodimers after DFT refinement and the single-point intramolecular SCS-MP2D energy correction. The monomer, SGD, and SSRD structures are indicated. Overlays comparing the predicted (green) and experimental (gray) monomer, SGD, and SSRD structures, along with their corresponding rmsd15 values, are also shown.

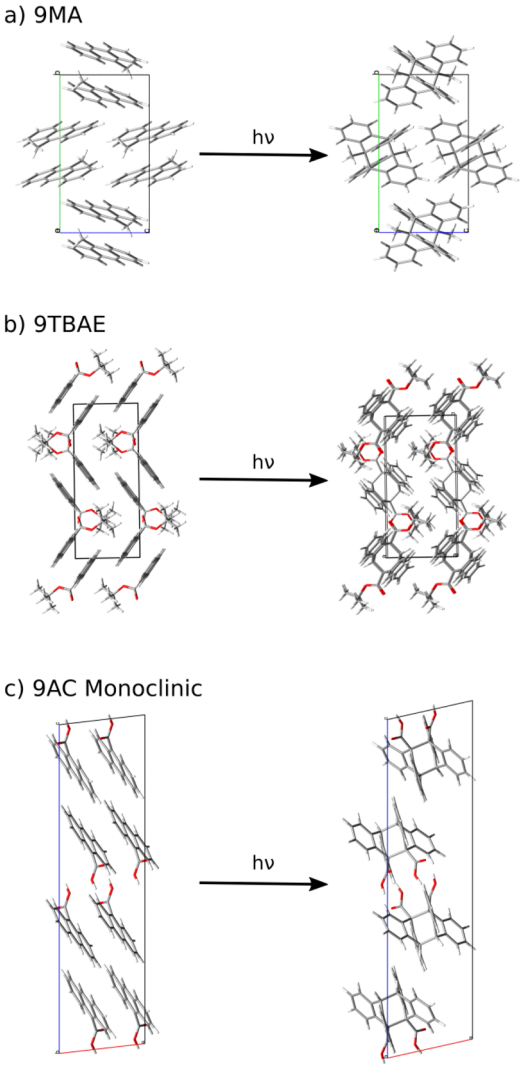

Fig. 3 The crystalline topochemical hypothesis generates the SSRD based on the crystal packing of the monomer, as shown here for (a) **9MA**, (b) **9TBAE**, and (c) **9AC**.

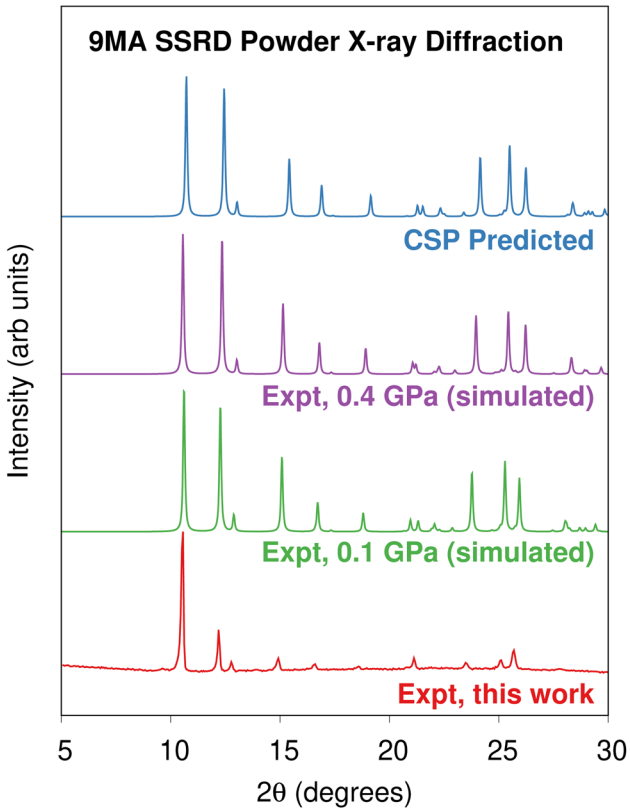

Fig. 4 Comparison of the powder X-ray diffractograms obtained on platelets of **9MA** after 40 seconds illumination against the powder diffractograms simulated using the experimentally-reported[85] SSRD crystal structures obtained at 0.1 and 0.4 GPa and the SSRD structure generated *via* crystal structure prediction here.

relative peak intensities are different from those in the calculated PXRD pattern. Peak positions match within 0.2°, which is consistent with the differences in volumes between the different experimental pressures and 0 K DFT calculations. Furthermore, the peak with enhanced intensity at 10.6° corresponds to the 001/100 Miller planes, which lie parallel to the *bc* crystal plane and thus horizontal along the substrate. The preferred orientation of the crystals should lead to enhanced intensity of this peak, as observed. Interestingly, after photoconversion the experimental SSRD pattern disappears over the course of 1 hour as the plates become almost completely amorphous (ESI Fig. S4†). Waiting for 5 days or heating the **9MA** sample did not lead to recrystallization into the low energy SGD form, suggesting there is a considerable barrier to reorder the molecules into this polymorph. The rapid loss of the SSRD structure suggests that it is highly unstable. Previously, we observed that **9MA** powders appeared to transform directly from monomer to the SGD photodimer structure.[19] We suspect that the sample preparation process used in that work, which involved grinding the crystals after UV irradiation, facilitated the SSRD-to-SGD transition and caused us to miss the presence of the SSRD intermediate. All these observations are consistent with the SSRD being a high-energy polymorph that can be stabilized by the application of mechanical pressure.

The **9MA** monomer to SSRD structural transformation is anisotropic: the DFT-calculated cell contracts 2.6% and 3.7% along the *a* and *b* crystallographic axes, but it expands by 5.9% along *c* and the monoclinic angle β increases by 3.2% (Fig. 5a). The calculated expansions and contractions are slightly less than observed experimentally in the **9MA** microplates,[89] which may be a consequence of temperature effects since the calculations were done at 0 K. The large elongation along the *c* axis stems from an increase in lateral spacing between photodimers, rather than from the butterflying of the anthracene rings upon photodimerization. Energetically, the SSRD lies a rather large 10.1 kJ mol^{-1} above both the monomer and SGD crystal structures. Previous polymorphism surveys suggest that only ~1–3% of polymorph pairs differ by 10 kJ mol^{-1} or more, and such large energy differences are even less common for rigid molecules such as **9MA** and its photodimer.[61,90,91]

Overall, both crystal structure prediction and the *in silico* topochemical SSRD formation approach independently produce the same SSRD structure. The topochemical approach

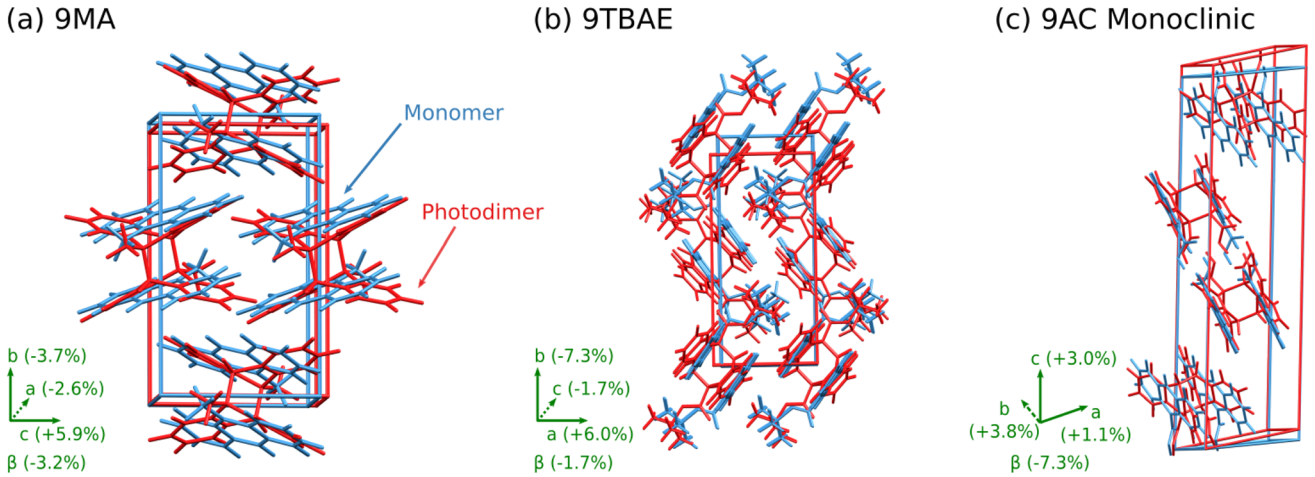

Fig. 5 Structure overlays showing the unit cell transformation from monomer (blue) to SSRD (red) for (a) **9MA**, (b) **9TBAE**, and (c) monoclinic **9AC**.

identifies the SSRD based on its relationship to the monomer crystal, while full predicted crystal energy landscape of the photodimer provides confirmation of that structure and its energy relative to other observed and/or predicted photodimer polymorphs. Together with the successful prediction of the monomer and SGD crystals, these results demonstrate that the important **9MA** crystal structures and the solid-state photochemical transformation can be predicted entirely from first-principles.

3.1.2 9TBAE. Next, we further validate our crystalline topochemical approach by determining the solid-state photochemical transformations in **9TBAE**. For simplicity, we omit the full crystal structure prediction steps. Instead, we start from the experimentally-known monomer crystal structure, relax it with DFT, and then predict the associated topochemical SSRD structures.

Previous NMR crystallography work established the structure of the **9TBAE** SSRD as an ensemble of six, closely related and dynamically interconverting structures that differ only subtly in the torsional angles of the *tert*-butyl groups.[92] Applying the topochemical approach to the **9TBAE** monomer (Fig. 3b) predicts a $P2_1/n$ SSRD structure that is similar to those six structures identified in the earlier study. Although the topochemical SSRD here retains the monoclinic symmetry of its parent monomer crystal, it overlaps with the six experimentally inferred orthorhombic structures with rmsd15 values around 0.4 Å. Further confirmation of the topochemically-predicted SSRD comes from the X-ray diffraction structure for a partially photodimerized **9TBAE** crystal.[18] Extracting photodimer components from that partially-reacted experimental structure and relaxing them with DFT produces a $P2_1/n$ symmetry structure in excellent agreement with the topochemically predicted one (rmsd15 = 0.11 Å). See ESI Section S4† for additional analysis of these SSRD structures.

Structurally, solid-state photodimerization of **9TBAE** induces a much larger unit cell change than **9MA** (Fig. 5). The **9TBAE** unit cell expands 6.0% along the *a* axis, largely due to the butterflying motion of the anthracene rings. Simultaneously, the monomers sliding into register as they photodimerize leads to a 7.3% contraction along the *b* axis. The *c* and *β* lattice parameters change only slightly, and the net volume change is small. These structural changes are consistent with the mechanism and magnitudes of nanorod elongation observed previously.[6,93]

3.1.3 9AC. Now consider monoclinic **9AC**. Structural characterization of its SSRD has proved experimentally infeasible to-date due to the short photodimer lifetimes (seconds to minutes),[94,95] which makes theoretical predictions essential to understanding the transformation. Fig. 3c and 5c show the topochemically-predicted crystal transformation. Whereas the photodimerizations of **9MA** and **9TBAE** both involve substantial elongation along a crystallographic axis, monoclinic **9AC** exhibits only modest changes in the *a*, *b*, and *c* lattice parameters. Instead, the major transformation occurs *via* the 7.3% decrease in the *β* angle.

The one-dimensional stacking geometry in the **9AC** crystal is qualitatively different from the herringbone geometry seen in **9MA** and **9TBAE**. This leads to a very different morphology change. The lack of extension along a major crystal axis probably explains why it has been more difficult to detect length changes for **9AC** nanorods, although bending and twisting are much more readily observed.[94,96,97]

3.2 Photomechanical engine cycle

Now that the photochemical structural transformations are understood for all three systems, we need a conceptual framework to predict the work output. We establish an idealized four-step photochemical engine cycle (Fig. 6) that enables characterization of the work that could potentially be performed by a given material:

1. The cycle begins with an "instantaneous" and complete solid-state photodimerization of the monomer species, converting the equilibrium monomer crystal to the proto-SSRD. The proto-SSRD retains the monomer unit cell parameters and is therefore highly strained.

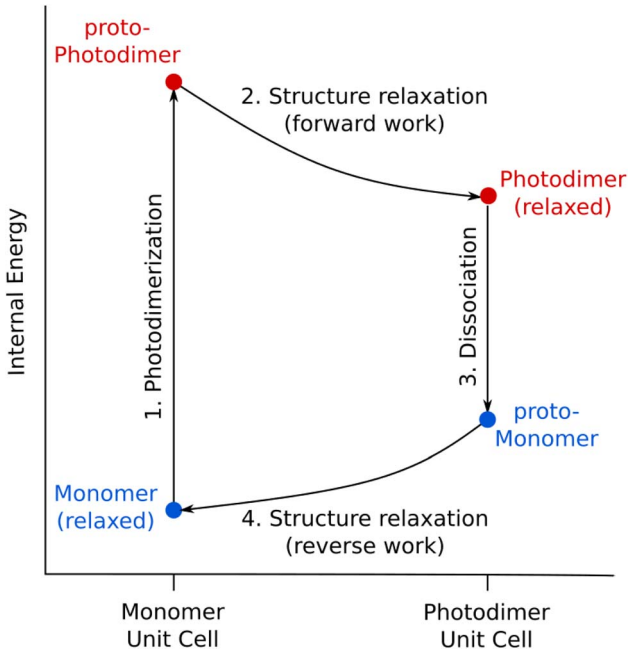

Fig. 6 The proposed photomechanical engine cycle for anthracene systems consists of: (1) topochemical photodimerization within the monomer unit cell to form the proto-photodimer (SSRD), (2) relaxation of the strained proto-photodimer to perform forward work, (3) topochemical dissociation of the photodimer back to the monomer within the photodimer unit cell (proto-monomer), and (4) reverse work generated by relaxation of the proto-monomer back to the original equilibrium structure.

2. The proto-SSRD relaxes to its equilibrium geometry. The associated stress release transforms the crystal structure anisotropically and produces "forward" mechanical work.

3. The photodimer dissociates to a strained proto-monomer—the monomer packed within the SSRD lattice parameters.

4. The proto-monomer relaxes back to the original equilibrium monomer crystal structure, producing mechanical work in the "reverse" direction.

In other words, chemical transformation creates the strained crystalline state, and relaxation of the associated stress produces work. Although the lattice parameter changes in Step 4 exactly mirror those from Step 2, the work performed in the forward and reverse directions will differ because the stress/elastic constants differ between the proto-SSRD and proto-monomer. In practice, this means that a photomechanical engine can perform net work similar to a traditional Carnot cycle based on gas expansion/compression. In the case of a photomechanical crystal, the input photon(s) act as an effective high temperature bath.

It is important to emphasize that real-world photomechanical crystals are expected to deviate from this idealized photochemical engine cycle. First, the solid-state photodimerization process does not occur instantly. Nevertheless, Raman spectroscopy experiments in certain photomechanical crystals suggest that the photochemical reaction and resulting crystal-to-crystal transformation do largely precede the relaxation of the unit cell.[98,99] Solid-state photochemical reactions can also exhibit cooperative kinetics due to the changing local crystalline environment as the mixture of reacted and unreacted species evolves.[100] However, such kinetic effects do not alter the final thermodynamic state achieved after complete reaction of the crystal and are therefore ignored in this idealized engine model.

Second, the solid-state photochemical reaction may not always reach 100% completion, whether due to positive photochromism or crystal packing reasons. For example, photodimerization within the one-dimensional monomer stacks in monoclinic **9AC** occurs stochastically and only reaches ~75% completion, with the remaining monomers becoming isolated and unable to react.[97,101] Crystal defects, impurities, and the experimental light source can also impact the extent of reaction.

Third, many photomechanical processes are not reversible in practice. For example, the **9MA** SSRD transforms to an amorphous material instead of reverting back to the monomer (ESI Fig. S3†), while the **9TBAE** SSRD slowly converts to the SGD.[18] On the other hand, **9AC** photodimerization is thermally reversible on the timescale of minutes.[97] In other photochromic and photomechanical crystals, the reverse reaction can be triggered *via* a different wavelength of light[102,103] or external pressure.[104]

Despite these caveats, the idealized photomechanical engine cycle presented here provides a useful framework for quantifying the nature and magnitude of work that could hypothetically be performed by the system and for comparing the photomechanical responses of different materials.

3.3 Photomechanical performance

Having defined the photomechanical engine cycle, we analyze the photomechanical performance of **9MA**, **9TBAE**, and monoclinic **9AC**. There are several different energies that are involved in the photomechanical cycle. We first consider the energetics of the photochemical reaction itself. The computed solid-state photodimerization reaction energies differ significantly across **9MA**, **9TBAE**, and **9AC**. **9MA** photodimerization is the least endothermic at 10.1 kJ mol^{-1}. For **9TBAE**, the photodimerization energy increases to 32.1 kJ mol^{-1}, reflecting the steric penalty of the bulky *tert*-butyl ester groups. The **9TBAE** SSRD is computed here to lie 12.0 kJ mol^{-1} above the SGD, similar to what was found previously.[61] On the other hand, the 101.2 kJ mol^{-1} photodimerization energy for monoclinic **9AC** is several-times larger than the other two systems. The constraints of maintaining the hydrogen-bonded tetramer units within the **9AC** lattice make this solid-state reaction energy even larger than the already endothermic **9AC** gas-phase photodimerization.[95] The highly endothermic forward reaction in **9AC** could imply a relatively small reverse reaction thermal barrier in accord with the Hammond postulate. This might explain why **9AC** photodimerization is thermally reversible, unlike **9MA** and **9TBAE**. However, detailed investigation of the reaction kinetics is beyond the scope of the present study. In any case, all of these endothermic reaction energies are small relative to the 300 kJ mol^{-1} energy input provided by the 400 nm photons driving the dimerization.

In our photomechanical engine framework, the actual mechanical work is done not by the photoreaction, but by the

subsequent relaxation of the crystal lattice to accommodate the newly formed photoproduct. Fig. 7 presents the energies for each step of the cycle in each species, while Fig. 8 plots the corresponding anisotropic work densities for the forward photodimerization (Step 2) and reverse dissociation (Step 4) portions of the engine cycle.

Consider first the forward photodimerization process in **9MA**. The proto-SSRD lies 21.9 kJ mol^{-1} above the equilibrium monomer crystal. Relaxation of the proto-SSRD unit cell to its equilibrium geometry stabilizes it by 11.8 kJ mol^{-1} (for a net reaction energy of 10.1 kJ mol^{-1}). Fig. 8a plots the computed elastic work produced by relaxation of the proto-SSRD. The maximal 25.0 MJ m^{-3} work density occurs roughly along the *c* axis, which is unsurprising given the large 5.4% elongation in that direction. Much less work is produced by the smaller contractions along the *a* and *b* axis.

While **9MA** does not exhibit solid-state photochemical reversibility experimentally, we can examine what would happen if it completed the photomechanical engine cycle. The proto-monomer formed *via* dissociation within the photodimer unit cell lattice parameters is 0.7 kJ mol^{-1} more stable than the SSRD, and it relaxes 9.4 kJ mol^{-1} back to the original monomer unit cell. So while the lattice parameter changes upon dissociation mirror those from the photodimerization, the smaller stress and relaxation energy associated with photodimer dissociation translate to a maximum elastic work density of only 12.3 MJ m^{-3} for Step 4 of the engine cycle (Fig. 8b) that is half as large as the forward (Step 2) work.

9TBAE exhibits somewhat larger energy changes than **9MA** throughout the engine cycle (Fig. 7). At the same time, the maximum forward-direction work density of 46.7 MJ m^{-3} for **9TBAE** (Fig. 8c) is nearly double that of **9MA**. Notably, the 6.0% expansion along the *a* axis produces far more work than the 8.5% contraction along the *b*. The *a* expansion reflects the bending out of the anthracene rings, while the *b* contraction stems from the energetically "softer" compression of the void space created as the monomer units slide into register to react.

As noted earlier, photodimerization of monoclinic **9AC** is highly endothermic. The proto-SSRD lies 119.1 kJ mol^{-1} above the monomer, compared to 21.9 and 61.0 kJ mol^{-1} for **9MA** and **9TBAE**, respectively. However, the 17.9 kJ mol^{-1} relaxation energy of the **9AC** proto-SSRD is intermediate between that of **9MA** (11.8 kJ mol^{-1}) and **9TBAE** (31.5 kJ mol^{-1}). Correspondingly, the maximal work density of 30.1 in the forward direction is closer to that of **9MA** than that of **9TBAE** (Fig. 8e). Whereas the maximal work density for **9MA** and **9TBAE** is performed along a crystallographic axis, the maximal work density in **9AC** occurs in between the *a* and *c* axes—it stems largely from the 7.3% contraction of the β angle upon photodimerization. As for **9MA**, the reverse work resulting from the photodimer dissociations in **9TBAE** and **9AC** are substantially smaller than for the forward photodimerizations (Fig. 8d and f).

Taken together, these results reveal several important features of these photomechanical crystals: first, the model predicts photomechanical crystal work densities of ~10^7 J m^{-3}, which is several orders of magnitude larger than the experimental work densities that have been reported experimentally to-date for thermosalient and photomechanical organic crystal actuators (~10–10^5 J m^{-3})[13,81,105] or photomechanical polymers (up to ~10^5 J m^{-3}).[13,106] It will be important to see if future experiments can confirm these high predicted work densities. Second, the work resulting from the photodimerization is roughly double that produced by the dissociation. This reflects how the anthracene monomer crystals deform much more readily (*i.e.* with less stress) than the photodimer ones. Third, the anisotropic structural changes produce work that is also

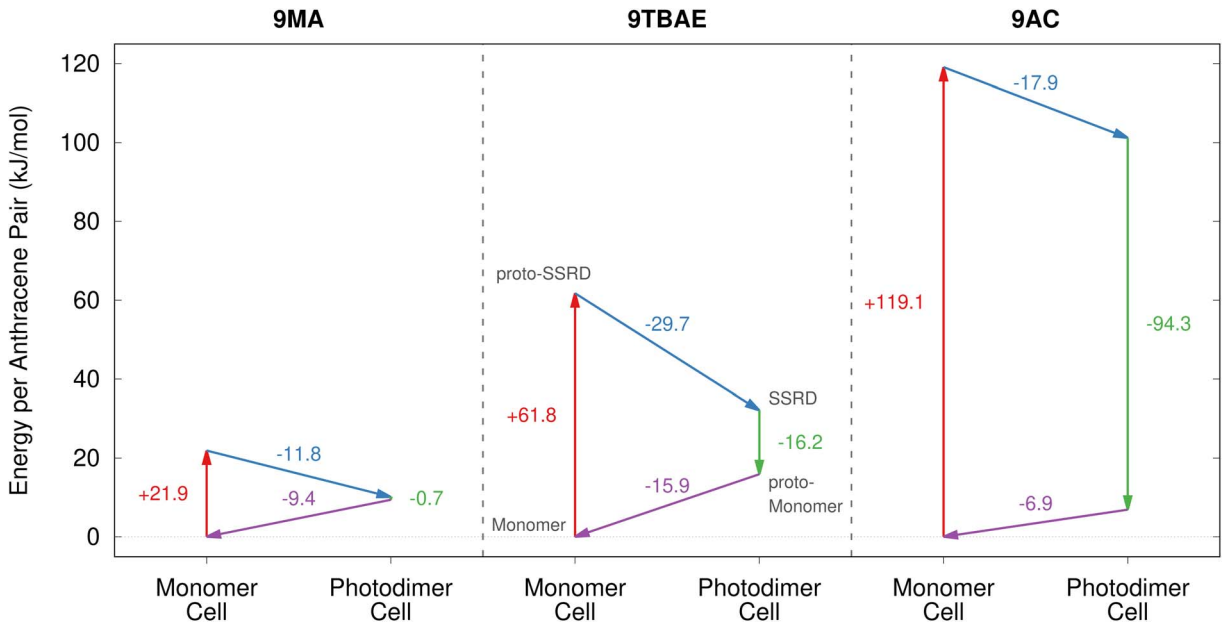

Fig. 7 The energetics associated with the four stages of the photomechanical engine cycle differ significantly across **9MA**, **9TBAE**, and monoclinic **9AC**.

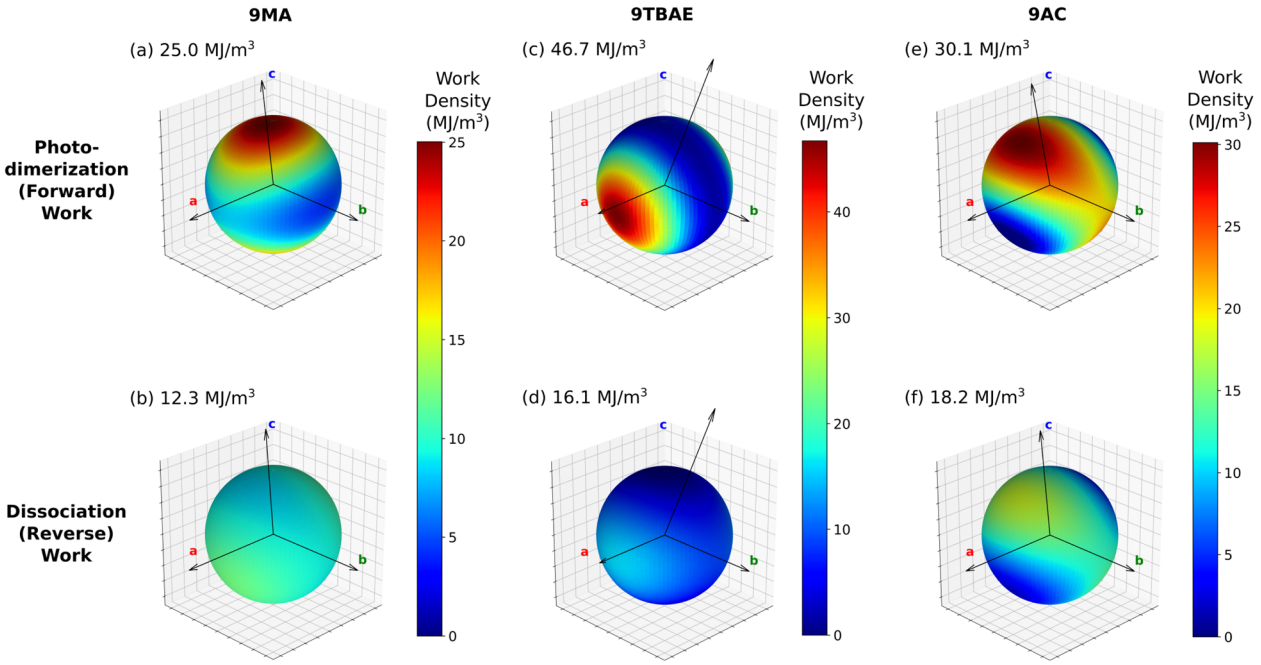

Fig. 8 The predicted work densities for the forward photodimerization and reverse dissociation reactions of **9MA**, **9TBAE**, and monoclinic **9AC** are highly anisotropic. Crystallographic axis shown correspond to the unit cell of the product for each reaction, and the maximal computed work density for each transformation is indicated. Absolute values of the work densities are plotted for convenience.

highly anisotropic. This highlights the importance of crystal morphology and orientation for device performance. Fourth, the amount of the work performed by a switchable photomechanical material cannot always be inferred from the crystallographic change in lattice parameters (strain) alone; the stress component of the work also depends significantly on the molecular packing. This is evident in the disparities seen for the **9TBAE** work densities along the *a* and *b* axes and in the differences between the forward and reverse directions for all three systems. Fifth, the reaction energetics are somewhat decoupled from the amount of photomechanical work performed. **9AC** photodimerization is much more endothermic than the other two species, but **9TBAE** can perform considerably more mechanical work. This suggests that it may be possible to design materials that tune the reaction reversibility and the photomechanical work semi-independently.

Finally, we briefly consider the photon-to-work efficiencies of these photomechanical engine cycles. Based on the ~12–30 kJ mol^{-1} Step 2 relaxation energies per reactive pair in the engine cycle (Fig. 7), ~5–10% of the input 400 nm (300 kJ mol^{-1}) photon energy is converted to forward work. Subtracting the energy change from the reverse direction (Fig. 7, Step 4), we estimate that ~1–5% of the input photon energy is converted to net work. Of course, given the anisotropy of the structure transformation and its resulting work, not all of that relaxation energy will translate into the forward/reverse work for a given actuator mode. Nevertheless, the efficiencies will likely remain in the range of a few percent for these photomechanical engines. For comparison, experimental photon-to-work efficiencies up to 0.1% have been determined for the bending motions of azobenzenes,[13] though they are frequently much lower for photomechanical actuators.[13,107] At the other extreme, a simple 1-D model suggests that efficiencies of up to 55% are achievable in principle.[108]

3.4 Future prospects for rational design

Looking forward, the techniques described here create, for the first time, the opportunity to design new photomechanical derivatives *in silico*. To do so, one might perform crystal structure prediction for a series of reactant species to identify the most stable crystal structure(s), the potential for polymorphism,[109] and to what extent the stable crystal packings satisfy topochemical constraints for the desired solid-state reactions.

Assuming that the photochemistry is not prevented by steric or excitonic effects in the crystal, the photochemical transformation and mechanical properties can be computed inexpensively from the reactant crystal structures, as demonstrated here for **9TBAE** and **9AC**. Anisotropic work density calculations can provide guidance on the potential performance of a material and how one should design an actuator that maximizes the work performed for a desired task. For example, to lift an object from below using a linear actuator, one might focus on forward expansion work and let gravity facilitate the reverse contraction process. On the other hand, linear contraction work could be used to lift an object from above. From Fig. 5 and 8, we can see that the same crystal can be used for both types of work simply by changing its orientation with respect to the load. For the most promising species, one might obtain further insights into the viability, stability, and reversibility of the system by

exploring the full crystal energy landscape of the photoproduct and assessing the reaction energetics and structural relationships among different photoproduct polymorphs (*e.g.* SSRD *vs.* SGD).[61,95]

4 Conclusions

This study demonstrates how solid-state photochemical transformations in organic crystals can be predicted entirely from first principles. It addresses several long-standing challenges surrounding the design of solid-state photoswitching and photomechanical systems, including the difficulties associated with determining the crystal structures of the photoproducts, with anticipating how changes to molecular structures will impact the crystal structures, and with understanding how crystal structure determines the mechanical response properties. The proposed photomechanical engine cycle provides a framework for characterizing the anisotropic photomechanical responses in these systems. It can be used to identify which crystal orientations or morphologies can best exploit the work produced by the photochemical transformation and to compare the potential for photomechanical work across different materials.

While the present study focuses on anthracene-based crystals, these same techniques can readily be applied to other solid-state photoswitching crystals, such as azobenzenes and diarylethenes. The detailed atomistic pictures generated with these techniques could also provide the foundation for multiscale models[13] that could predict photomechanical behaviors in nanoscale actuators and would facilitate the development of practical organic crystal engines.

Data availability

All relevant data is included in the ESI† materials already.

Author contributions

Beran conceived the research project with Bardeen, with additional input from Mueller and Al-Kaysi. The computational studies and data analysis were carried out by Cook and Beran. The experimental studies and data analysis were performed by Li, Lui, and Gately, under Bardeen's supervision. The manuscript was primarily written by Beran and Bardeen, with contributions from the other authors.

Conflicts of interest

There are no conflicts to declare.

Acknowledgements

G. J. O. B. acknowledges support from the National Science Foundation (CHE-1955554) and supercomputer time from XSEDE (TG-CHE110064), C. J. B. acknowledges support from the Office of Naval Research (MURI on Photomechanical Material Systems; ONR N00014-18-1-2624), and L. J. M. acknowledges support from the National Institutes of Health (R35GM145369). We thank Alex Greaney for helpful discussions.

Notes and references

1 P. Naumov, D. P. Karothu, E. Ahmed, L. Catalano, P. Commins, J. Mahmoud Halabi, M. B. Al-Handawi and L. Li, *J. Am. Chem. Soc.*, 2020, **142**, 13256–13272.
2 T. Kim, L. Zhu, R. O. Al-Kaysi and C. J. Bardeen, *ChemPhysChem*, 2014, **15**, 400–414.
3 P. Naumov, S. Chizhik, M. K. Panda, N. K. Nath and E. Boldyreva, *Chem. Rev.*, 2015, **115**, 12440–12490.
4 *Photomechanical Materials, Composites, and Systems*, ed. T. J. White, Wiley, Chichester, UK, 2017.
5 *Mechanically Responsive Materials for Soft Robotics*, ed. H. Koshima, Wiley, 2020.
6 R. O. Al-Kaysi, A. M. Müller and C. J. Bardeen, *J. Am. Chem. Soc.*, 2006, **128**, 15938–15939.
7 S. Kobatake, S. Takami, H. Muto, T. Ishikawa and M. Irie, *Nature*, 2007, **446**, 778–781.
8 M. Morimoto and M. Irie, *J. Am. Chem. Soc.*, 2010, **132**, 14172–14178.
9 H. Koshima, N. Ojima and H. Uchimoto, *J. Am. Chem. Soc.*, 2009, **131**, 6890–6891.
10 O. S. Bushuyev, A. Tomberg, T. Friščić and C. J. Barrett, *J. Am. Chem. Soc.*, 2013, **135**, 12556–12559.
11 H. Wang, P. Chen, Z. Wu, J. Zhao, J. Sun and R. Lu, *Angew. Chem., Int. Ed.*, 2017, **56**, 9463–9467.
12 P. Naumov, J. Kowalik, K. M. Solntsev, A. Baldridge, J.-S. Moon, C. Kranz and L. M. Tolbert, *J. Am. Chem. Soc.*, 2010, **132**, 5845–5857.
13 J. Mahmoud Halabi, E. Ahmed, S. Sofela and P. Naumov, *Proc. Nat. Acad. Sci.*, 2021, **118**, 1–7.
14 D. Kitagawa, H. Tsujioka, F. Tong, X. Dong, C. J. Bardeen and S. Kobatake, *J. Am. Chem. Soc.*, 2018, **140**, 4208–4212.
15 A. Colin-Molina, D. P. Karothu, M. J. Jellen, R. A. Toscano, M. A. Garcia-Garibay, P. Naumov and B. Rodríguez-Molina, *Matter*, 2019, **1**, 1033–1046.
16 D.-K. Bučar and L. R. MacGillivray, *J. Am. Chem. Soc.*, 2007, **129**, 32–33.
17 A. E. Keating and M. A. Garcia-Garibay, *Photochemical Solid-To-Solid Reaction in Organic and Inorganic Photochemistry*, eds. Ramamurthy, V. and Schanze, K., Marcel Dekker, New York, 1998, vol. 2, pp. 195–248.
18 L. Zhu, A. Agarwal, J. Lai, R. O. Al-Kaysi, F. S. Tham, T. Ghaddar, L. Mueller and C. J. Bardeen, *J. Mater. Chem.*, 2011, **21**, 6258–6268.
19 T. Kim, L. Zhu, L. J. Mueller and C. J. Bardeen, *J. Am. Chem. Soc.*, 2014, **136**, 6617–6625.
20 D. Kitagawa and S. Kobatake, *J. Phys. Chem. C*, 2013, **117**, 20887–20892.
21 N. K. Nath, L. Pejov, S. M. Nichols, C. Hu, N. Saleh, B. Kahr and P. Naumov, *J. Am. Chem. Soc.*, 2014, **136**, 2757–2766.
22 G. J. O. Beran, *Chem. Rev.*, 2016, **116**, 5567–5613.
23 S. Grimme, A. Hansen, J. G. Brandenburg and C. Bannwarth, *Chem. Rev.*, 2016, **116**, 5105–5154.

24 J. Hoja, A. M. Reilly and A. Tkatchenko, *Wiley Interdiscip. Rev.: Comput. Mol. Sci.*, 2017, **7**, e1294.
25 J. Hermann, R. A. DiStasio and A. Tkatchenko, *Chem. Rev.*, 2017, **117**, 4714–4758.
26 A. Otero-De-La-Roza, B. H. Cao, I. K. Price, J. E. Hein and E. R. Johnson, *Angew. Chem., Int. Ed.*, 2014, **53**, 7879–7882.
27 S. R. Whittleton, A. Otero-de-la Roza and E. R. Johnson, *J. Chem. Theory Comput.*, 2017, **13**, 441–450.
28 S. R. Whittleton, A. Otero-de-la Roza and E. R. Johnson, *J. Chem. Theory Comput.*, 2017, **13**, 5332–5342.
29 D. E. Braun, J. A. McMahon, L. H. Koztecki, S. L. Price and S. M. Reutzel-Edens, *Cryst. Growth Des.*, 2014, **14**, 2056–2072.
30 D. E. Braun, S. R. Lingireddy, M. D. Beidelschies, R. Guo, P. Müller, S. L. Price and S. M. Reutzel-Edens, *Cryst. Growth Des.*, 2017, **17**, 5349–5365.
31 D. E. Braun, J. A. McMahon, R. M. Bhardwaj, J. Nyman, M. A. Neumann, J. Van De Streek and S. M. Reutzel-Edens, *Cryst. Growth Des.*, 2019, **19**, 2947–2962.
32 D. H. Case, V. K. Srirambhatla, R. Guo, R. E. Watson, L. S. Price, H. Polyzois, J. K. Cockcroft, A. J. Florence, D. A. Tocher and S. L. Price, *Cryst. Growth Des.*, 2018, **18**, 5322–5331.
33 E. Schur, J. Bernstein, L. S. Price, R. Guo, S. L. Price, S. H. Lapidus and P. W. Stephens, *Cryst. Growth Des.*, 2019, **19**, 4884–4893.
34 M.-A. Perrin, M. A. Neumann, H. Elmaleh and L. Zaske, *Chem. Commun.*, 2009, 3181–3183.
35 A. Asmadi, M. A. Neumann, J. Kendrick, P. Girard, M. A. Perrin and F. J. J. Leusen, *J. Phys. Chem. B*, 2009, **113**, 16303–16313.
36 A. D. Bond, K. A. Solanko, J. van de Streek and M. A. Neumann, *CrystEngComm*, 2011, **13**, 1768.
37 G. R. Woollam, M. A. Neumann, T. Wagner and R. J. Davey, *Faraday Discuss.*, 2018, **211**, 209–234.
38 J. Hoja and A. Tkatchenko, *Faraday Discuss.*, 2018, **211**, 253–274.
39 J. Hoja, H.-Y. Ko, M. A. Neumann, R. Car, R. A. DiStasio and A. Tkatchenko, *Sci. Adv.*, 2019, **5**, eaau3338.
40 M. Mortazavi, J. Hoja, L. Aerts, L. Quéré, J. van de Streek, M. A. Neumann and A. Tkatchenko, *Commun. Chem.*, 2019, **2**, 70.
41 G. Sun, X. Liu, Y. A. Abramov, S. O. Nilsson Lill, C. Chang, V. Burger and A. Broo, *Cryst. Growth Des.*, 2021, **21**, 1972–1983.
42 C. Greenwell, J. L. McKinley, P. Zhang, Q. Zeng, G. Sun, B. Li, S. Wen and G. J. O. Beran, *Chem. Sci.*, 2020, **11**, 2200–2214.
43 C. Greenwell and G. J. O. Beran, *Cryst. Growth Des.*, 2020, **20**, 4875–4881.
44 G. J. O. Beran, I. J. Sugden, C. Greenwell, D. H. Bowskill, C. C. Pantelides and C. S. Adjiman, *Chem. Sci.*, 2022, **13**, 1288–1297.
45 G. M. Day, T. G. Cooper, A. J. Cruz-Cabeza, K. E. Hejczyk, H. L. Ammon, S. X. M. Boerrigter, J. S. Tan, R. G. Della Valle, E. Venuti, J. Jose, S. R. Gadre, G. R. Desiraju, T. S. Thakur, B. P. van Eijck, J. C. Facelli, V. E. Bazterra, M. B. Ferraro, D. W. M. Hofmann, M. A. Neumann, F. J. J. Leusen, J. Kendrick, S. L. Price, A. J. Misquitta, P. G. Karamertzanis, G. W. A. Welch, H. A. Scheraga, Y. A. Arnautova, M. U. Schmidt, J. van de Streek, A. K. Wolf and B. Schweizer, *Acta Cryst. B*, 2009, **65**, 107–125.
46 D. A. Bardwell, C. S. Adjiman, Y. A. Arnautova, E. Bartashevich, S. X. M. Boerrigter, D. E. Braun, A. J. Cruz-Cabeza, G. M. Day, R. G. Della Valle, G. R. Desiraju, B. P. van Eijck, J. C. Facelli, M. B. Ferraro, D. Grillo, M. Habgood, D. W. M. Hofmann, F. Hofmann, K. V. J. Jose, P. G. Karamertzanis, A. V. Kazantsev, J. Kendrick, L. N. Kuleshova, F. J. J. Leusen, A. V. Maleev, A. J. Misquitta, S. Mohamed, R. J. Needs, M. A. Neumann, D. Nikylov, A. M. Orendt, R. Pal, C. C. Pantelides, C. J. Pickard, L. S. Price, S. L. Price, H. A. Scheraga, J. van de Streek, T. S. Thakur, S. Tiwari, E. Venuti and I. K. Zhitkov, *Acta Cryst. B*, 2011, **67**, 535–551.
47 A. M. Reilly, R. I. Cooper, C. S. Adjiman, S. Bhattacharya, A. D. Boese, J. G. Brandenburg, P. J. Bygrave, R. Bylsma, J. E. Campbell, R. Car, D. H. Case, R. Chadha, J. C. Cole, K. Cosburn, H. M. Cuppen, F. Curtis, G. M. Day, R. A. DiStasio Jr, A. Dzyabchenko, B. P. van Eijck, D. M. Elking, J. A. van den Ende, J. C. Facelli, M. B. Ferraro, L. Fusti-Molnar, C.-A. Gatsiou, T. S. Gee, R. de Gelder, L. M. Ghiringhelli, H. Goto, S. Grimme, R. Guo, D. W. M. Hofmann, J. Hoja, R. K. Hylton, L. Iuzzolino, W. Jankiewicz, D. T. de Jong, J. Kendrick, N. J. J. de Klerk, H.-Y. Ko, L. N. Kuleshova, X. Li, S. Lohani, F. J. J. Leusen, A. M. Lund, J. Lv, Y. Ma, N. Marom, A. E. Masunov, P. McCabe, D. P. McMahon, H. Meekes, M. P. Metz, A. J. Misquitta, S. Mohamed, B. Monserrat, R. J. Needs, M. A. Neumann, J. Nyman, S. Obata, H. Oberhofer, A. R. Oganov, A. M. Orendt, G. I. Pagola, C. C. Pantelides, C. J. Pickard, R. Podeszwa, L. S. Price, S. L. Price, A. Pulido, M. G. Read, K. Reuter, E. Schneider, C. Schober, G. P. Shields, P. Singh, I. J. Sugden, K. Szalewicz, C. R. Taylor, A. Tkatchenko, M. E. Tuckerman, F. Vacarro, M. Vasileiadis, A. Vazquez-Mayagoitia, L. Vogt, Y. Wang, R. E. Watson, G. A. de Wijs, J. Yang, Q. Zhu and C. R. Groom, *Acta Cryst. B*, 2016, **72**, 439–459.
48 M. A. Neumann, J. van de Streek, F. P. A. Fabbiani, P. Hidber and O. Grassmann, *Nat. Commun.*, 2015, **6**, 7793.
49 A. G. Shtukenberg, C. T. Hu, Q. Zhu, M. U. Schmidt, W. Xu, M. Tan and B. Kahr, *Cryst. Growth Des.*, 2017, **17**, 3562–3566.
50 A. G. Shtukenberg, M. Tan, L. Vogt-Maranto, E. J. Chan, W. Xu, J. Yang, M. E. Tuckerman, C. T. Hu and B. Kahr, *Cryst. Growth Des.*, 2019, **19**, 4070–4080.
51 E. L. Stevenson, R. W. Lancaster, A. B. M. Buanz, L. S. Price, D. A. Tocher and S. L. Price, *CrystEngComm*, 2019, **21**, 2154–2163.
52 S. Askin, J. K. Cockcroft, L. S. Price, A. D. Gonçalves, M. Zhao, D. A. Tocher, G. R. Williams, S. Gaisford and D. Q. M. Craig, *Cryst. Growth Des.*, 2019, **19**, 2751–2757.
53 A. N. Sokolov, S. Atahan-Evrenk, R. Mondal, H. B. Akkerman, R. S. Sánchez-Carrera, S. Granados-Focil,

J. Schrier, S. C. Mannsfeld, A. P. Zoombelt, Z. Bao and A. Aspuru-Guzik, *Nat. Commun.*, 2011, **2**, 437.
54 E. O. Pyzer-Knapp, H. P. G. Thompson, F. Schiffmann, K. E. Jelfs, S. Y. Chong, M. A. Little, A. I. Cooper and G. M. Day, *Chem. Sci.*, 2014, **5**, 2235–2245.
55 E. H. Wolpert and K. E. Jelfs, *Chem. Sci.*, 2022, **13**, 13588–13599.
56 A. Pulido, L. Chen, T. Kaczorowski, D. Holden, M. A. Little, S. Y. Chong, B. J. Slater, D. P. McMahon, B. Bonillo, C. J. Stackhouse, A. Stephenson, C. M. Kane, R. Clowes, T. Hasell, A. I. Cooper and G. M. Day, *Nature*, 2017, **543**, 657–664.
57 P. Cui, D. P. McMahon, P. R. Spackman, B. M. Alston, M. A. Little, G. M. Day and A. I. Cooper, *Chem. Sci.*, 2019, **10**, 9988–9997.
58 R. L. Greenaway, V. Santolini, A. Pulido, M. A. Little, B. M. Alston, M. E. Briggs, G. M. Day, A. I. Cooper and K. E. Jelfs, *Angew. Chem., Int. Ed.*, 2019, **58**, 16275–16281.
59 C. Y. Cheng, J. E. Campbell and G. M. Day, *Chem. Sci.*, 2020, **11**, 4922–4933.
60 Q. Zhu, J. Johal, D. E. Widdowson, Z. Pang, B. Li, C. M. Kane, V. Kurlin, G. M. Day, M. A. Little and A. I. Cooper, *J. Am. Chem. Soc.*, 2022, **144**, 9893–9901.
61 G. J. O. Beran, *CrystEngComm*, 2019, **21**, 758–764.
62 P. J. Stephens, F. J. Devlin, C. F. Chabalowski and M. J. Frisch, *J. Phys. Chem.*, 1994, **98**, 11623–11627.
63 M. J. Frisch, G. W. Trucks, H. B. Schlegel, G. E. Scuseria, M. A. Robb, J. R. Cheeseman, G. Scalmani, V. Barone, B. Mennucci, G. A. Petersson, H. Nakatsuji, M. Caricato, X. Li, H. P. Hratchian, A. F. Izmaylov, J. Bloino, G. Zheng, J. L. Sonnenberg, M. Hada, M. Ehara, K. Toyota, R. Fukuda, J. Hasegawa, M. Ishida, T. Nakajima, Y. Honda, O. Kitao, H. Nakai, T. Vreven, J. A. Montgomery Jr, J. E. Peralta, F. Ogliaro, M. Bearpark, J. J. Heyd, E. Brothers, K. N. Kudin, V. N. Staroverov, R. Kobayashi, J. Normand, K. Raghavachari, A. Rendell, J. C. Burant, S. S. Iyengar, J. Tomasi, M. Cossi, N. Rega, J. M. Millam, M. Klene, J. E. Knox, J. B. Cross, V. Bakken, C. Adamo, J. Jaramillo, R. Gomperts, R. E. Stratmann, O. Yazyev, A. J. Austin, R. Cammi, C. Pomelli, J. W. Ochterski, R. L. Martin, K. Morokuma, V. G. Zakrzewski, G. A. Voth, P. Salvador, J. J. Dannenberg, S. Dapprich, A. D. Daniels, Ö. Farkas, J. B. Foresman, J. V. Ortiz, J. Cioslowski and D. J. Fox, *Gaussian 09 Revision E.01*, Gaussian Inc, Wallingford CT, 2009.
64 S. Fredericks, K. Parrish, D. Sayre and Q. Zhu, *Comput. Phys. Comm.*, 2021, **261**, 107810.
65 J. Wang, R. M. Wolf, J. W. Caldwell, P. A. Kollman and D. A. Case, *J. Comp. Chem.*, 2004, **25**, 1157–1174.
66 B. R. Brooks, C. L. Brooks, A. D. Mackerell, L. Nilsson, R. J. Petrella, B. Roux, Y. Won, G. Archontis, C. Bartels, S. Boresch, A. Caflisch, L. Caves, Q. Cui, A. R. Dinner, M. Feig, S. Fischer, J. Gao, M. Hodoscek, W. Im, K. Kuczera, T. Lazaridis, J. Ma, V. Ovchinnikov, E. Paci, R. W. Pastor, C. B. Post, J. Z. Pu, M. Schaefer, B. Tidor, R. M. Venable, H. L. Woodcock, X. Wu, W. Yang, D. M. York and M. Karplus, *J. Comp. Chem.*, 2009, **30**, 1545–1614.
67 R. Sure and S. Grimme, *J. Comp. Chem.*, 2013, **34**, 1672–1685.
68 R. Dovesi, A. Erba, R. Orlando, C. M. Zicovich-Wilson, B. Civalleri, L. Maschio, M. Rérat, S. Casassa, J. Baima, S. Salustro and B. Kirtman, *Wiley Interdiscip. Rev.: Comput. Mol. Sci.*, 2018, **8**, e1360.
69 A. D. Becke, *J. Chem. Phys.*, 1986, **85**, 7184–7187.
70 J. P. Perdew, K. Burke and M. Ernzerhof, *Phys. Rev. Lett.*, 1996, **77**, 3865.
71 A. Otero-de-la Roza and E. R. Johnson, *J. Chem. Phys.*, 2012, **136**, 174109.
72 P. Giannozzi, O. Andreussi, T. Brumme, O. Bunau, M. Buongiorno Nardelli, M. Calandra, R. Car, C. Cavazzoni, D. Ceresoli, M. Cococcioni, N. Colonna, I. Carnimeo, A. Dal Corso, S. de Gironcoli, P. Delugas, R. A. DiStasio, A. Ferretti, A. Floris, G. Fratesi, G. Fugallo, R. Gebauer, U. Gerstmann, F. Giustino, T. Gorni, J. Jia, M. Kawamura, H.-Y. Ko, A. Kokalj, E. Küçükbenli, M. Lazzeri, M. Marsili, N. Marzari, F. Mauri, N. L. Nguyen, H.-V. Nguyen, A. Otero-de-la Roza, L. Paulatto, S. Poncé, D. Rocca, R. Sabatini, B. Santra, M. Schlipf, A. P. Seitsonen, A. Smogunov, I. Timrov, T. Thonhauser, P. Umari, N. Vast, X. Wu and S. Baroni, *J. Phys. Condens. Mat.*, 2017, **29**, 465901.
73 S. Grimme, C. Diedrich and M. Korth, *Angew. Chem., Int. Ed.*, 2006, **45**, 625–629.
74 J. Řezáč, C. Greenwell and G. J. O. Beran, *J. Chem. Theory Comput.*, 2018, **14**, 4711–4721.
75 C. Greenwell, J. Řezáč and G. J. O. Beran, *Phys. Chem. Chem. Phys.*, 2022, **24**, 3695–3712.
76 A. J. Cohen, P. Mori-Sánchez and W. Yang, *Chem. Rev.*, 2012, **112**, 289–320.
77 L. M. LeBlanc, S. G. Dale, C. R. Taylor, A. D. Becke, G. M. Day and E. R. Johnson, *Angew. Chem., Int. Ed.*, 2018, **57**, 14906–14910.
78 A. Otero-de-la Roza, L. M. LeBlanc and E. R. Johnson, *J. Chem. Theory Comput.*, 2019, **15**, 4933–4944.
79 C. Greenwell and G. J. O. Beran, *J. Mater. Chem. C*, 2021, **9**, 2848–2857.
80 G. J. O. Beran, S. E. Wright, C. Greenwell and A. J. Cruz-Cabeza, *J. Chem. Phys.*, 2022, **156**, 104112.
81 D. P. Karothu, J. Mahmoud Halabi, L. Li, A. Colin-Molina, B. Rodríguez-Molina and P. Naumov, *Adv. Mater.*, 2020, **32**, 1906216.
82 A. F. Mabied, M. Müller, R. E. Dinnebier, S. Nozawa, M. Hoshino, A. Tomita, T. Sato and S. I. Adachi, *Acta Crystallogr., Sect. B: Struct. Sci.*, 2012, **68**, 424–430.
83 J. A. Chisholm and W. D. S. Motherwell, *J. Appl. Crystallogr.*, 2005, **38**, 228–231.
84 J. L. McKinley and G. J. O. Beran, *J. Chem. Theory Comput.*, 2019, **15**, 5259–5274.
85 J. Bakowicz and I. Turowska-Tyrk, *Acta Cryst. B*, 2022, **78**, 223–230.
86 H. Ihmels, D. Leusser, M. Pfeiffer and D. Stalke, *Tetrahedron*, 2000, **56**, 6867–6875.

87 W. N. Wang and W. Jones, *Mol. Cryst. Liq. Cryst. Sci. Technol., Sect. A*, 1994, **242**, 227–240.
88 I. Turowska-Tyrk and E. Trzop, *Acta Cryst. B*, 2003, **59**, 779–786.
89 K. Morimoto, D. Kitagawa, F. Tong, K. Chalek, L. J. Mueller, C. J. Bardeen and S. Kobatake, *Angew. Chem., Int. Ed.*, 2022, **61**, e202114089.
90 J. Nyman and G. M. Day, *CrystEngComm*, 2015, **17**, 5154–5165.
91 A. J. Cruz-Cabeza, S. M. Reutzel-Edens and J. Bernstein, *Chem. Soc. Rev.*, 2015, **44**, 8619–8635.
92 C. Yang, L. Zhu, R. A. Kudla, J. D. Hartman, R. O. Al-Kaysi, S. Monaco, B. Schatschneider, A. Magalhaes, G. J. O. Beran, C. J. Bardeen and L. J. Mueller, *CrystEngComm*, 2016, **18**, 7319–7329.
93 K. R. Chalek, X. Dong, F. Tong, R. A. Kudla, L. Zhu, A. D. Gill, W. Xu, C. Yan, J. D. Hartman, A. Magalhaes, R. O. Al-Kaysi, R. C. Hayward, R. J. Hooley, G. J. O. Beran, C. J. Bardeen and L. J. Mueller, *Chem. Sci.*, 2021, **12**, 453–463.
94 L. Zhu, F. Tong, C. Salinas, M. K. Al-Muhanna, F. S. Tham, D. Kisailus, R. O. Al-Kaysi and C. J. Bardeen, *Chem. Mater.*, 2014, **26**, 6007–6015.
95 T. J. Gately, W. Sontising, C. J. Easley, I. Islam, R. O. Al-Kaysi, G. J. O. Beran and C. J. Bardeen, *CrystEngComm*, 2021, **23**, 5931–5943.
96 R. O. Al-Kaysi and C. J. Bardeen, *Adv. Mater.*, 2007, **19**, 1276–1280.
97 L. Zhu, R. O. Al-Kaysi and C. J. Bardeen, *J. Am. Chem. Soc.*, 2011, **133**, 12569–12575.
98 T. Salzillo and A. Brillante, *CrystEngComm*, 2019, **21**, 3127–3136.
99 T. Salzillo, I. Bilotti, R. G. Della Valle, E. Venuti and A. Brillante, *J. Am. Chem. Soc.*, 2012, **134**, 17671–17679.
100 K. Morimoto, D. Kitagawa, C. J. Bardeen and S. Kobatake, *Chem. Eur. J.*, 2022, DOI: **10.1002/chem.202203291**.
101 R. Moré, G. Busse, J. Hallmann, C. Paulmann, M. Scholz and S. Techert, *J. Phys. Chem. C*, 2010, **114**, 4142–4148.
102 M. Irie, T. Fukaminato, K. Matsuda and S. Kobatake, *Chem. Rev.*, 2014, **114**, 12174–12277.
103 O. Sato, *Nat. Chem.*, 2016, **8**, 644–656.
104 S. R. Jezowski, L. Zhu, Y. Wang, A. P. Rice, G. W. Scott, C. J. Bardeen and E. L. Chronister, *J. Am. Chem. Soc.*, 2012, **134**, 7459–7466.
105 D. P. Karothu, R. Ferreira, G. Dushaq, E. Ahmed, L. Catalano, J. M. Halabi, Z. Alhaddad, I. Tahir, L. Li, S. Mohamed, M. Rasras and P. Naumov, *Nat. Commun.*, 2022, **13**, 2823.
106 T. H. Ware, M. E. McConney, J. J. Wie, V. P. Tondiglia and T. J. White, *Science*, 2015, **347**, 982–984.
107 X. Dong, F. Tong, K. M. Hanson, R. O. Al-Kaysi, D. Kitagawa, S. Kobatake and C. J. Bardeen, *Chem. Mater.*, 2019, **31**, 1016–1022.
108 A. J. Berges and C. J. Bardeen, *Photochem. Photobiol. Sci.*, 2022, **21**, 1845–1852.
109 S. L. Price, D. E. Braun and S. M. Reutzel-Edens, *Chem. Commun.*, 2016, **52**, 7065–7077.